chemistry proceedings

MDPI

Proceeding Paper

Investigation of Detector Technology Alternatives in Cone Beam CT—A Simulation Study †

Evangelia Karali *, Christos Michail, George Fountos, Nektarios Kalyvas and Ioannis Valais

Radiation Physics, Materials Technology and Biomedical Imaging Laboratory, Department of Biomedical Engineering, University of West Attica, Ag. Spyridonos, 12210 Athens, Greece; cmichail@uniwa.gr (C.M.); gfoun@uniwa.gr (G.F.); nkalyvas@uniwa.gr (N.K.); valais@uniwa.gr (I.V.)

* Correspondence: ekarali@uniwa.gr

† Presented at the 5th International Online Conference on Crystals, 15–17 June 2026; Available online: https://sciforum.net/event/IOCC2026.

Abstract

Cone beam CT (CBCT) is an excellent alternative to mammography in breast imaging. CBCT detector technology is based on CsI:Tl (cesium iodine) material. Due to CsI:Tl performance limitations in photon-counting CBCT, a question arises whether another material could be more effective. In order to find an optimum detector configuration in terms of MTF (modulation transfer function) and DQE (detective quantum efficiency), a micro-CBCT system was simulated in GATE v.9.2, incorporating eight different detector configurations. GAGG demonstrated a 10% increase in spatial resolution and a 4% increase in DQE compared to commonly used CsI. Similar results were obtained from FBP and OS-SIRT reconstructed images. GAGG is a strong candidate for CBCT detectors, offering improved spatial resolution, image quality and matching in SiPM readout systems.

Keywords: CBCT; photon counting detectors; GAGG; CZT; breast imaging; scintillators; semiconductors; GATE; microcalcifications

1. Introduction

The classification of microcalcifications into Type I and Type II determines whether malignant pathology is present. Timely diagnosis of breast cancer in a non-invasive way requires detecting microcalcifications with good resolution and reliably distinguishing between Type I and Type II microcalcifications in imaging [1].

Cone beam CT (CBCT) is an excellent alternative to mammography in breast imaging since the breast is uncompressed while CBCT image quality is adequate, even in a dense breast. CBCT technology is based on a detector technology that uses a scintillator (e.g., thallium-activated cesium iodide, CsI:Tl) to convert X-ray energy into light, which is then followed by standard light-to-electric pulse converters. CsI:Tl shows high light output performance of over 60,000 ph/MeV at room temperature. Its light emission range (peaking at 560 nm) matches well with the spectral sensitivity of photodiodes. CsI:Tl has a rather slow response to X-ray photons. Its response time constant (0.6–0.9 μs) may be insufficient for high photon-count X-ray imaging applications, and even with the Tl activator, it is a partially hygroscopic scintillator. This restricts its use in high-humidity conditions. Additionally, CsI:Tl exhibits high levels of afterglow during scintillation decay, which causes image blurring in high-speed imaging applications [2].

Recent research on CBCT detector configuration has explored photon counting detector technology adapted from nuclear medicine. A key question is whether an optimum detector

Check for updates

Academic Editor: John Parthenios

Published: 4 November 2026

Copyright: © 2026 by the authors. Licensee MDPI, Basel, Switzerland. This article is an open access article distributed under the terms and conditions of the Creative Commons Attribution (CC BY) license.

configuration exists in terms of MTF (modulation transfer function), which describes spatial resolution, and DQE (detective quantum efficiency), which reflects the overall signal-to-noise ratio transfer from input to output. DQE can be improved by using high-Z detector materials with a density higher than CsI crystal [2].

In this study, eight different CBCT possible detector configurations were simulated in GATE [3], and tomographic images were derived and evaluated. Spatial resolution was examined using MTF curves, detector signal-to-noise ratio transfer was investigated using DQE and microcalcification visibility was assessed using CNRs (contrast-to-noise ratios). The purpose was to find an optimum detector configuration for low-count CBCT breast imaging. Table 1 summarizes detector materials used, accompanied by their properties, presenting typical ranges reported in the literature. These values may vary depending on the crystal vendor, doping, thickness, readout sensor, shaping time and measurement energy [4]. Material properties are based on published literature [4–6]. Linear attenuation coefficients at 40 keV are estimated using NIST XCOM data [7], while photon attenuation percentages for a 1 mm thickness are calculated as $(100(1\text{-}e^{-\mu t}))$, where t = 0.1 cm. These materials were selected to investigate scintillators with different physical and optical properties, while CZT was included as a representative direct-conversion semiconductor detector.

Table 1. Detector materials and their imaging properties [4,7].

Material	Detector Type	Density (g/cm^3)	Effective Z	Linear Attenuation Coefficient at 40 keV (cm^{-1})	Estimated X-Ray Absorption (1 mm, 40 keV)	Lateral Signal-Spread Mechanism	K-Edge (keV)	Hygroscopic
CsI:Tl	Scintillator	~4.5	~54	~29–31	~94–95%	Optical light spread (structure-dependent)	I: 33.2	Slightly
LSO:Ce	Scintillator	~7.4	~66	~55–60	>99%	Optical photon transport	Lu: 63.3	No
LYSO:Ce	Scintillator	~7.1	~65	~53–58	>99%	Optical photon transport	Lu: 63.3	No
BGO	Scintillator	~7.1	~75	~70–75	>99.9%	Optical photon transport	Bi: 90.5	No
$LaBr_3$:Ce	Scintillator	~5.1	~47	~20–24	~88–91%	Optical photon transport	La: 38.9	Yes
GAGG:Ce	Scintillator	~6.6	~54	~38–42	~97–98%	Optical photon transport	Gd: 50.2	No
LuAG:Ce	Scintillator	~6.7	~59	~42–46	~98–99%	Optical photon transport	Lu: 63.3	No
CZT	Direct semi-conductor	~5.8–6.0	~49–50	~30–35	~95–97%	Charge diffusion and sharing	Cd: 26.7, Te: 31.8	No

GATE is a Monte Carlo platform that is suitable for nuclear medical imaging systems and CT (Computed Tomography) simulation. It has been widely validated with real clinical and experimental systems [8,9].

2. Materials and Methods

2.1. The Micro CBCT System

A micro CBCT was simulated in GATE [3] based on a 6.8° aperture micro-focus X-ray source. The activity of a source was set to 0.35 MBq, since GATE v.9.2.1 requires source radioactivity for PET, SPECT and CT systems to be determined. The source spectrum was extended to 40 keV. The micro CBCT system had a rotated table 15 cm away from the source, rotating from 0 to 359° with a rotation step of 1°. The detector configuration was 15.05 cm away from the table, 50 × 50 × 1 mm^3 in size, and discretized into 100 × 100 × 1 pixels (so pixel size was 0.5 × 0.5 × 1 mm^3). The geometric magnification is 2. The simulated setup is presented in Figure 1.

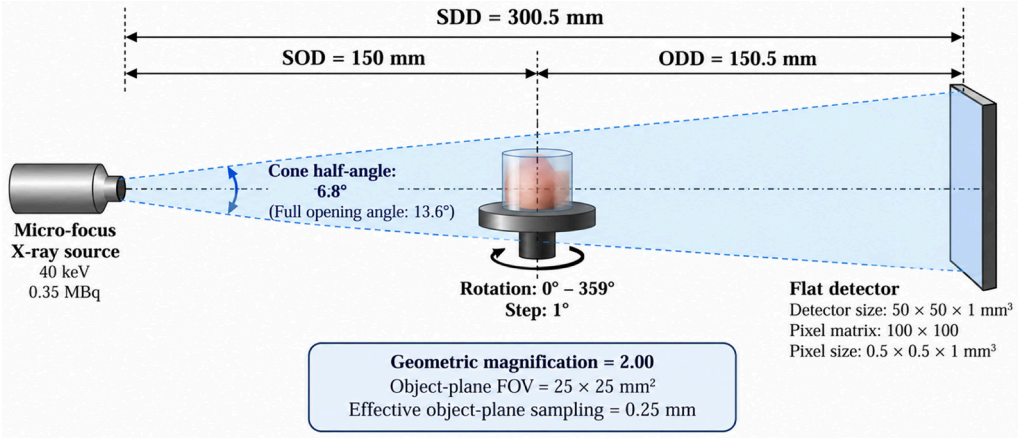


Figure 1. A schematic representation of the CBCT simulated setup.

The acquisition was performed using 1 s/projection. A total of 360 angular projections were collected. So, approximately 3.5×10^5 primary photon histories were generated per projection, corresponding to approximately 1.26×10^8 primary histories over the complete scan, for all detector configurations. Based on the source-to-detector geometry and the angular emission cone, approximately 2.18×10^5 photons per projection were incident on the 50×50 mm^2 detector area, corresponding to an average incident fluence of approximately 87 photons/mm^2 per projection.

The detector consists either of a scintillation material coupled to a realistic generic SiPM (silicon photomultiplier tube) or of a semiconductor. Seven different scintillation materials were used, namely bismuth germanate (BGO), lutetium oxyorthosilicate (LSO:Ce), lutetium–yttrium oxyorthosilicate (LYSO:Ce) (both doped with Ce), CsI:Tl (doped with Tl), gadolinium aluminum gallium garnet (GAGG:Ce), lanthanum bromide ($LaBr_3$:Ce) and Lutetium aluminum garnet (LuAG). These crystals were coupled to a SiPM. The SiPM was based on a pixel-level readout. Spatial blurring was set to 0.55 mm and the energy resolution was set to 10% at 30 keV. A 10–40 keV energy acceptance window to simulate the detector response under low-energy X-ray imaging conditions was applied. Apart from scintillators, a cadmium zinc telluride (CZT) semiconductor was also assessed. CZT was applied with generic CZT signal processing characteristics, namely pixel readout, 0.25 mm spatial blurring and 6% energy resolution at 30 keV, with accepted events restricted to the 10–40 keV energy range [4].

Data were stored in .txt format. Each script contained data from one angle view. Image size (in planar and tomographic mode) was set to 128 × 128 pixels.

2.2. Phantoms

In order to evaluate the eight different detector configurations, three phantoms were simulated. An aluminum capillary 0.5 mm in diameter was used so that MTF (modulation transfer function) curves could be extracted along with MTF10 [10], defined as the frequency at which the MTF decreases to 10% of its zero-frequency value, reflecting the system's spatial resolution. A cylindrical water phantom was also simulated to evaluate NPS (noise power spectrum) and to extract NPS radial profiles. MTF data together with NPS radial profile data were used to determine the system's DQE. Finally, a dense breast phantom containing microcalcifications was further used to assess the system's image quality. All three phantoms were specifically designed and implemented in GATE for the present study, with their geometries and dimensions illustrated in Figure 2. The dense-breast phantom containing HAp and $CaCO_3$ microcalcifications was designed for evaluating lesion contrast and detectability under controlled imaging conditions.

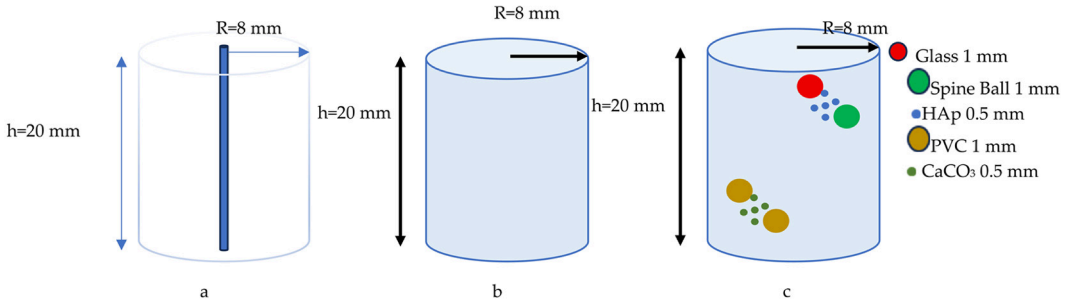


Figure 2. (**a**) Aluminum capillary, (**b**) water cylinder, (**c**) dense breast phantom with microcalcifications.

2.3. Data Processing

Images were processed in planar and tomographic mode. Tomographic data were reconstructed using FBP (filtered backprojection algorithm) [11], applying a Hanning window for sinogram data filtering and bilinear interpolation at the image level. Data were also reconstructed with OS-SIRT (ordered-subsets simultaneous iterative reconstruction technique) [12] using 2 iterations and 24 subsets. OS-SIRT combines the ordered-subsets strategy with simultaneous iterative reconstruction to improve convergence speed while preserving image quality in limited-count CBCT data. The system matrix needed for the OS-SIRT procedure was implemented as presented in [13].

2.4. Detector/Image Quality Metrics

MTF curves were extracted as the Fourier transform of a PSF (point spread function) profile of the capillary image. Spatial resolution was measured at MTF10 [10]. The capillary image was bilinearly interpolated to a 256 × 256 grid to improve numerical sampling of the line-spread function prior to Fourier transformation. However, this did not extend the physical Nyquist limit.

The NPS [14] is a key metric for describing the type and level of noise in imaging systems. It quantifies how the noise variance is distributed as a function of spatial frequency. The radial NPS profile was calculated from the 2D NPS profile extracted from the water-cylinder phantom.

DQE [14] is the most concise measure of how effectively an imaging system converts incoming photons into a useful image. It measures, as a function of spatial frequency, how well information (resolution) is preserved relative to noise. It is typically written as $DQE(f) = SNRout^2/SNRin^2$ and in practice is estimated from MTF(f) and NPS(f) or NNPS(f) along with q_0 (the number of photons hitting the detector per area), so $DQE(f) = MTF(f)^2/(q_0 \cdot NNPS(f))$. High DQE means that for the same dose/exposure, you get better image quality as frequency increases. DQE is affected by pixel size, scattering within the crystal and in the light detector, the data acquisition protocol, and the image reconstruction algorithm. For OS-SIRT reconstructed data, DQE was not used. Image quality was derived from CNR ratios. CNR ratios for tomographic data were calculated as described in [13].

3. Results

3.1. Planar Data

Figure 3 presents MTF and 1D radial NPS profile curves, while Figure 4 presents DQE curves for each detector configuration. GAGG material presents a spatial resolution of 1.59 cycles/mm, a value that is about 10% higher in comparison to CsI. The 1D radial NPS profile demonstrates a sharp increase in noise power at very low spatial frequencies, followed by a relatively flat spectrum up to the Nyquist limit (2 cycles/mm), which indicates that the

noise in the planar plane is not strongly "colored" under these specific conditions and spatial frequencies. NPS is calculated for the cylindrical water phantom using a homogeneous ROI (region of interest) 35 × 35 pixels in size. The ensemble mean was estimated from all projection images and subtracted from each individual projection to isolate stochastic noise. Then the two-dimensional Fourier transform of the noise image was extracted. The resulting two-dimensional NPS was ensemble-averaged over all projections and radially averaged to obtain the one-dimensional NPS profile. This was subsequently normalized to produce the NNPS used for DQE calculation. The GAGG DQE maximum (0.86) is almost 4% higher than the CsI DQE maximum (0.825). Table 2 provides an overview of the results.

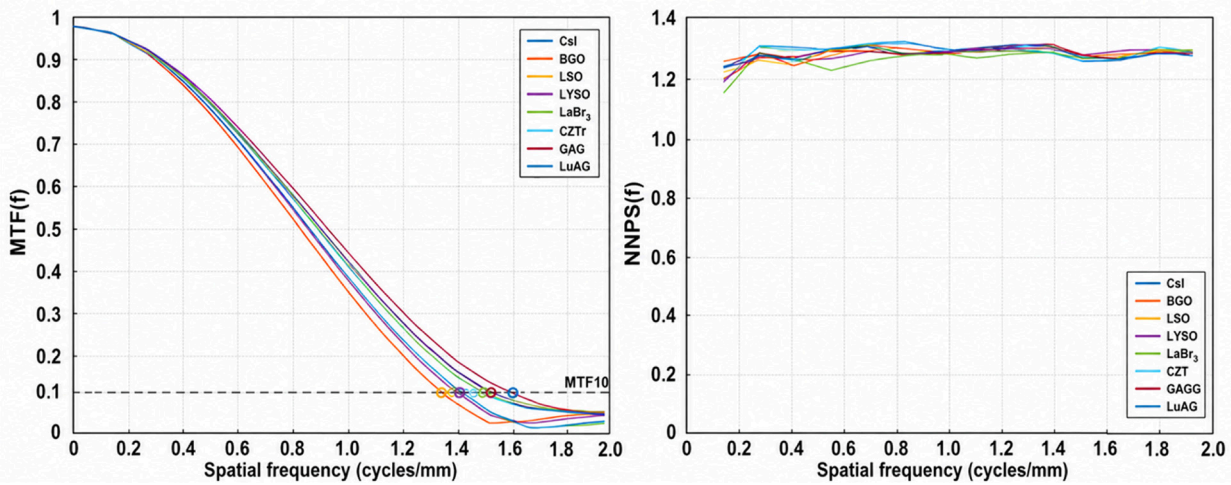


Figure 3. A superimposition of MTF curves (**left**) and 1D radial NPS profiles for every detector configuration.

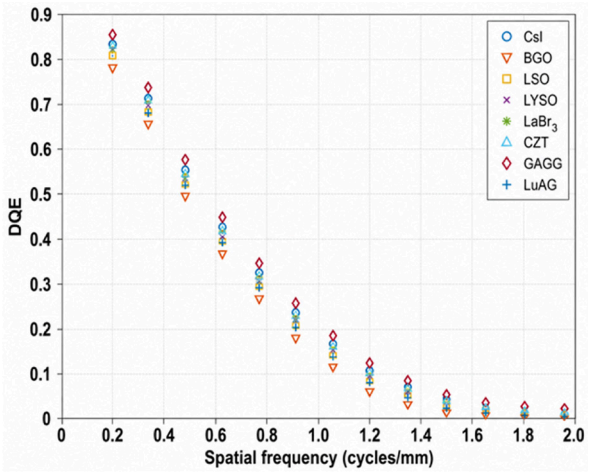


Figure 4. A superimposition of DQE curves for the eight detector configurations under investigation.

Table 2. MTF10, peak DQE, and DQE AUC of planar imaging performance across the eight simulated detector configurations.

Detector Material	MTF10 (Cycles/mm)	Peak DQE (Mean ± SD)	DQE AUC (Mean ± SD)
CsI:Tl	1.4865	0.8250 ± 0.0225	0.3706 ± 0.0044
BGO	1.3353	0.8217 ± 0.0218	0.3396 ± 0.0046
LSO	1.5163	0.8509 ± 0.0242	0.3902 ± 0.0049
LYSO	1.3804	0.8364 ± 0.0236	0.3572 ± 0.0044
$LaBr_3$	1.4112	0.8135 ± 0.0231	0.3604 ± 0.0045

Table 2. *Cont.*

Detector Material	MTF10 (Cycles/mm)	Peak DQE (Mean ± SD)	DQE AUC (Mean ± SD)
CZT	1.4060	0.8231 ± 0.0254	0.3579 ± 0.0048
GAGG:Ce	1.5923	0.8600 ± 0.0226	0.4044 ± 0.0049
LuAG	1.5160	0.8395 ± 0.0227	0.3897 ± 0.0043

Note: 300 bootstrap resamples of NPS; MTF held fixed. First two DQE frequency bins excluded from reported peak and AUC.

3.2. Tomographic Data

Tomographic images of slice #25, containing HAp microcalcifications, were reconstructed using FBP and OS-SIRT, as shown in Figure 5.

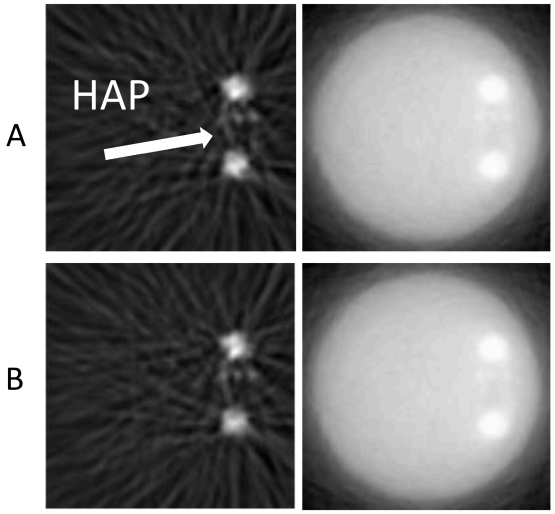


Figure 5. Tomographic images reconstructed with FBP and OS-SIRT, slice #25, acquired with (**A**) CsI and (**B**) GAGG detector material.

In Table 3, mean CNR values for each type of microcalcification are presented for tomographic slices #25 and #73 reconstructed with OS-SIRT and FBP.

Table 3. Mean CNRs for every detector configuration for breast phantom.

Material	Mean CNR HAp		Mean CNR $CaCO_3$	
	FBP	OS-SIRT	FBP	OS-SIRT
CsI	0.29	5.12	3.27	3.87
BGO	0.43	4.93	4.25	3.85
LSO	0.48	5.09	3.23	3.71
LYSO	0.44	4.96	4.60	3.82
$LaBr_3$	0.30	4.85	3.52	3.82
CZT	0.19	5.12	3.51	3.84
GAGG	0.50	5.33	4.73	3.98
LuAG	0.38	5.14	3.75	3.76

4. Discussion

GAGG exhibits the highest DQE and CNR while maintaining excellent spatial resolution. This material combines relatively high density, high light output, non-hygroscopic nature, and good compatibility with SiPM readouts [5]. It maintains efficient X-ray detection at different noise levels and distributions. Compared with the clinical reference

detector, CsI:Tl, GAGG:Ce demonstrated improved image quality in low-dose simulations. GAGG:Ce presents superior overall performance.

As far as CZT is concerned, it arises as the best detector technology choice for future breast CBCT systems due to its direct X-ray-to-electron conversion mechanism, excellent intrinsic spatial resolution, and potential for photon-counting and spectral imaging [6]. However, in this low-dose application study, CZT did not outperform the eight different detector materials. This is consistent with known limitations of pixelated CZT detectors, including charge-sharing, carrier-transport/charge-collection effects and electronic noise, which can degrade spatial and energy resolution and increase image noise [15]. In this study, all scintillators were attached to a generic SiPM-based readout model with spatial and energy resolution that resembles practical imaging systems. CZT detector was also simulated using representative direct-conversion detector characteristics. This approach enables a consistent comparison of currently available detector technologies under identical acquisition and reconstruction conditions. Thus, the observed differences arise from the material-dependent X-ray interaction and energy-deposition characteristics, including differences in elemental composition, density and X-ray attenuation. Image quality can also be affected by the reconstruction algorithm. OS-SIRT, being an iterative reconstruction procedure, reduces noise and improves microcalcifications' appearance in a dense breast phantom in comparison with the analytical FBP. However, detector performance remains unchanged; this suggests that it is mainly based on detector intrinsic characteristics.

5. Conclusions

GAGG:Ce demonstrated the best overall performance, offering improved spatial resolution, higher DQE than CsI and improved CNR under low-dose breast CBCT conditions. GAGG:Ce is a promising scintillator for future SiPM-based breast CBCT detectors. Further experimental studies are warranted to validate the simulation findings and investigate its clinical implementation. Compared with CZT, it is preferred for low-dose applications and is more cost-effective.

Author Contributions: Conceptualization, E.K. and C.M.; data curation, E.K., C.M., N.K., G.F. and I.V.; formal analysis, E.K., C.M., N.K., G.F. and I.V.; investigation, E.K., C.M., N.K., G.F. and I.V.; methodology, E.K., C.M., N.K., G.F. and I.V.; project administration, C.M. and I.V.; resources, C.M., G.F. and I.V.; software, E.K.; validation, C.M., N.K., G.F. and I.V.; visualization, E.K., C.M. and I.V.; writing—original draft, E.K., C.M., N.K., G.F. and I.V.; writing—review and editing, E.K., C.M., N.K., G.F. and I.V. All authors have read and agreed to the published version of the manuscript.

Funding: This research received no external funding.

Institutional Review Board Statement: Not applicable.

Informed Consent Statement: Not applicable.

Data Availability Statement: The data are contained within this article.

Conflicts of Interest: The authors declare no conflicts of interest.

Abbreviations

The following abbreviations are used in this manuscript:

CBCT	Cone beam computed tomography
CNR	Contrast-to-noise ratio
FBP	Filtered back-projection algorithm
OS-SIRT	Ordered subsets simultaneous iterative reconstruction technique
GATE	GEANT4 application for tomographic emission

References

1. Logullo, A.F.; Prigenzi, K.C.; Nimir, C.C.; Franco, A.F.; Campos, M.S. Breast microcalcifications: Past, present and future (Review). *Mol. Clin. Oncol.* **2022**, *16*, 81. [CrossRef] [PubMed]
2. Siddall, K.; Zhang, X.; O'Connell, A. Emerging Clinical Applications for Cone Beam Breast CT: Changing the Breast Imaging Paradigm. *Curr. Breast Cancer Rep.* **2024**, *16*, 134–141. [CrossRef]
3. OpenGATE Collaboration. GATE Documentation—GAM Documentation. Available online: https://opengate.readthedocs.io/_/downloads/en/v9.0/pdf/ (accessed on 7 June 2025).
4. Michail, C.; Liaparinos, P.; Kalyvas, N.; Kandarakis, I.; Fountos, G.; Valais, I. Phosphors and Scintillators in Biomedical Imaging. *Crystals* **2024**, *14*, 169. [CrossRef]
5. Dimitrakopoulos, A.; Michail, C.; Valais, I.; Fountos, G.; Kandarakis, I.; Kalyvas, N. Experimental Evaluation of GAGG:Ce Crystalline Scintillator Properties Under X-Ray Radiation. *Crystals* **2025**, *15*, 590. [CrossRef]
6. Makeev, A.; Clajus, M.; Snyder, S.; Wang, X.; Glick, S.J. Evaluation of position-estimation methods applied to CZT-based photon-counting detectors for dedicated breast CT. *J. Med. Imaging* **2015**, *2*, 023501. [CrossRef] [PubMed]
7. Berger, M.J.; Hubbell, J.H.; Seltzer, S.M.; Chang, J.; Coursey, J.S.; Sukumar, R.; Zucker, D.S.; Olsen, K. *XCOM: Photon Cross Sections Database, Version 1.5*; National Institute of Standards and Technology: Gaithersburg, MD, USA, 2010. Available online: https://www.nist.gov/pml/xcom-photon-cross-sections-database (accessed on 23 July 2026).
8. Lowther, N.; Myronakis, M.; Harris, T.; Berbeco, R.; Jacobson, M.; Etemadpour, R.; Ferguson, D.; Fueglistaller, R.; Arroyo, P.C.; Birrer, V.; et al. Validation of a Monte Carlo model of a large-format kV flat-panel system. *Med. Phys.* **2025**, *52*, e18093. [CrossRef] [PubMed]
9. McCabe, C.; Harrawood, B.; Samei, E.; Abadi, E. In silico modeling of a clinical photon-counting CT system: Verification and validation. *Med. Phys.* **2025**, *52*, 3840–3853. [CrossRef] [PubMed]
10. Samei, E.; Flynn, M.J.; Reimann, D.A. A method for measuring the presampled MTF of digital radiographic systems using an edge test device. *Med. Phys.* **1998**, *25*, 102–113. [CrossRef] [PubMed]
11. Herman, G.T. *Image Reconstruction from Projections: The Fundamentals of Computed Tomography*; Academic Press: New York, NY, USA, 1980.
12. Xu, F.; Xu, W.; Jones, M.; Keszthelyi, B.; Sedat, J.; Agard, D.; Mueller, K. On the efficiency of iterative ordered subset reconstruction algorithms for acceleration on GPUs. *Comput. Methods Programs Biomed.* **2010**, *98*, 261–270. [CrossRef] [PubMed]
13. Karali, E.; Michail, C.; Fountos, G.; Kalyvas, N.; Valais, I. Novel Detector Configurations in Cone-Beam CT Systems: A Simulation Study. *Crystals* **2024**, *14*, 416. [CrossRef]
14. Samei, E.; Ranger, N.T.; Dobbins, J.T.; Chen, Y. Report of AAPM Task Group 162: Software for Planar Image Quality Metrology. *Med. Phys.* **2018**, *45*, e32–e39. [CrossRef] [PubMed]
15. Bolotnikov, A.E.; Camarda, G.S.; Carini, G.A.; Cui, Y.; Kohman, K.T.; Li, L.; Salomon, M.B.; James, R.B. Performance-limiting defects in cdznte detectors. *IEEE Trans. Nucl. Sci.* **2007**, *54*, 821–827. [CrossRef]

Disclaimer/Publisher's Note: The statements, opinions and data contained in all publications are solely those of the individual author(s) and contributor(s) and not of MDPI and/or the editor(s). MDPI and/or the editor(s) disclaim responsibility for any injury to people or property resulting from any ideas, methods, instructions or products referred to in the content.